

See discussions, stats, and author profiles for this publication at: <https://www.researchgate.net/publication/262098106>

Analysis of Multi-valley and Multi-bandgap Absorption and Enhancement of Free Carriers Related to Exciton Screening in Hybrid Perovskites

ARTICLE in THE JOURNAL OF PHYSICAL CHEMISTRY C · MAY 2014

Impact Factor: 4.77 · DOI: 10.1021/jp503337a

CITATIONS

53

READS

315

3 AUTHORS:



J. Even

Institut National des Sciences Appliquées de R...

334 PUBLICATIONS 1,641 CITATIONS

SEE PROFILE



Laurent Pedesseau

Institut National des Sciences Appliquées de R...

116 PUBLICATIONS 485 CITATIONS

SEE PROFILE



Claudine Katan

French National Centre for Scientific Research

108 PUBLICATIONS 2,089 CITATIONS

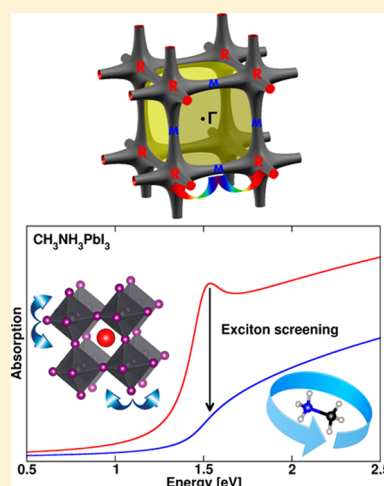
SEE PROFILE

Analysis of Multivalley and Multibandgap Absorption and Enhancement of Free Carriers Related to Exciton Screening in Hybrid Perovskites

Jacky Even,^{*,†} Laurent Pedesseau,[†] and Claudine Katan^{*,‡}[†]Université Européenne de Bretagne, INSA, FOTON, UMR 6082, 35708 Rennes, France[‡]CNRS, Institut des Sciences Chimiques de Rennes, UMR 6226, 35042 Rennes, France

S Supporting Information

ABSTRACT: Solution-processable metal–halide perovskites recently opened a new route toward low-cost manufacture of photovoltaic cells. Converting sunlight into electrical energy depends on several factors among which a broad absorption across the solar spectrum and attractive charge transport properties are of primary importance. Hybrid perovskites meet such prerequisites, but despite foremost experimental research efforts, their understanding remains scanty. Here we show that in these materials the appropriate absorption and transport properties are afforded by the multibandgap and multivalley nature of their band structure. We also investigate the nature of the photoexcited species. Our analysis suggests exciton screening by collective orientational motion of the organic cations at room temperature, leading to almost free carriers. Molecular collective motion is also expected to couple to carrier diffusion at room temperature. In mixed halides, our interpretation indicates that doping might hinder collective molecular motions, leading to good transport properties despite alloying and local lattice strain.



In a photovoltaic (PV) device, the conversion efficiency of solar radiation into electrical power is paramount. In 1961, Shockley and Queisser established the theoretical efficiency limit of an ideal single p–n junction solar cell, based on the principle of detailed balance.¹ This limit of 33.7% is almost attained by the best-performing heterojunctions.² Among the strategies developed to bypass this limit, concentrated multi-junction (multiple p–n junctions) PV cells^{2,3} undeniably afford upmost conversion efficiencies² but at the expense of elaborate and expensive growth modus operandi. Conversely, solution-processable metal–halide perovskites have recently opened a new route toward low-cost manufacture of solar cells.^{4–16} The tremendous research effort conducted during the last 2 years has mainly focused on the methylammonium lead-iodide perovskite ($\text{CH}_3\text{NH}_3\text{PbX}_3$, $\text{X} = \text{I}$). First used as the sensitizer in conventional dye sensitized solar cells,^{4–6} thanks to its good light harvesting abilities, its attractive charge transport properties allowed to achieve meso-superstructured solar cells (MSSC) and solid thin-film planar heterojunctions with record efficiencies up to 15%.^{7–15} In fact, broad absorption across the solar spectrum and appropriate electron and/or hole mobilities are prerequisites to high solar-to-electrical power conversion efficiencies. While there is clear experimental evidence that lead–halide perovskites meet these conditions, the understanding of underlying mechanism remains scarce.^{14–16} As Loi and Hummelen put forward, “it is now time to investigate the

physical properties that make hybrid perovskites so promising for solar-energy conversion.”¹⁶ First, the origin of the favorable light absorption over the visible to near-IR range is still mysterious in spite of a couple of recent theoretical investigations.^{17–23} At room temperature, the linear absorption spectrum of $\text{CH}_3\text{NH}_3\text{PbI}_3$ shows two absorption peaks located at 760 and 480 nm.^{14,15} Whereas the low energy peak was attributed to the direct bandgap transition from the valence band (VB) maximum to the conduction band (CB) minimum, the origin of the high-energy peak is clearly unresolved.¹⁵ Moreover, a hot hole cooling mechanism was also suggested for the intraband relaxation after optical excitation at high energy for $\text{CH}_3\text{NH}_3\text{PbI}_3$.¹⁵ Besides, halogen substitution ($\text{X}_3 = \text{I}_{3-x}\text{Cl}_x$ or $\text{I}_{3-x}\text{Br}_x$) has shown to provide improved transport properties and cell stability while preserving good performances including low fundamental energy losses.^{5,11–14} To understand such improvements, Snaith and colleagues have recently thoroughly investigated the carrier dynamics after optical excitation for $\text{X}_3 = \text{I}_{3-x}\text{Cl}_x$.²⁴ It is shown that after photoexcitation the second order transient THz transmission dynamics of triiodide compounds is an order of magnitude faster than for the mixed halide. Moreover, the latter exhibit larger mobilities (+43%), sizable enhancement of the absorption above the

Received: February 21, 2014

Published: May 6, 2014

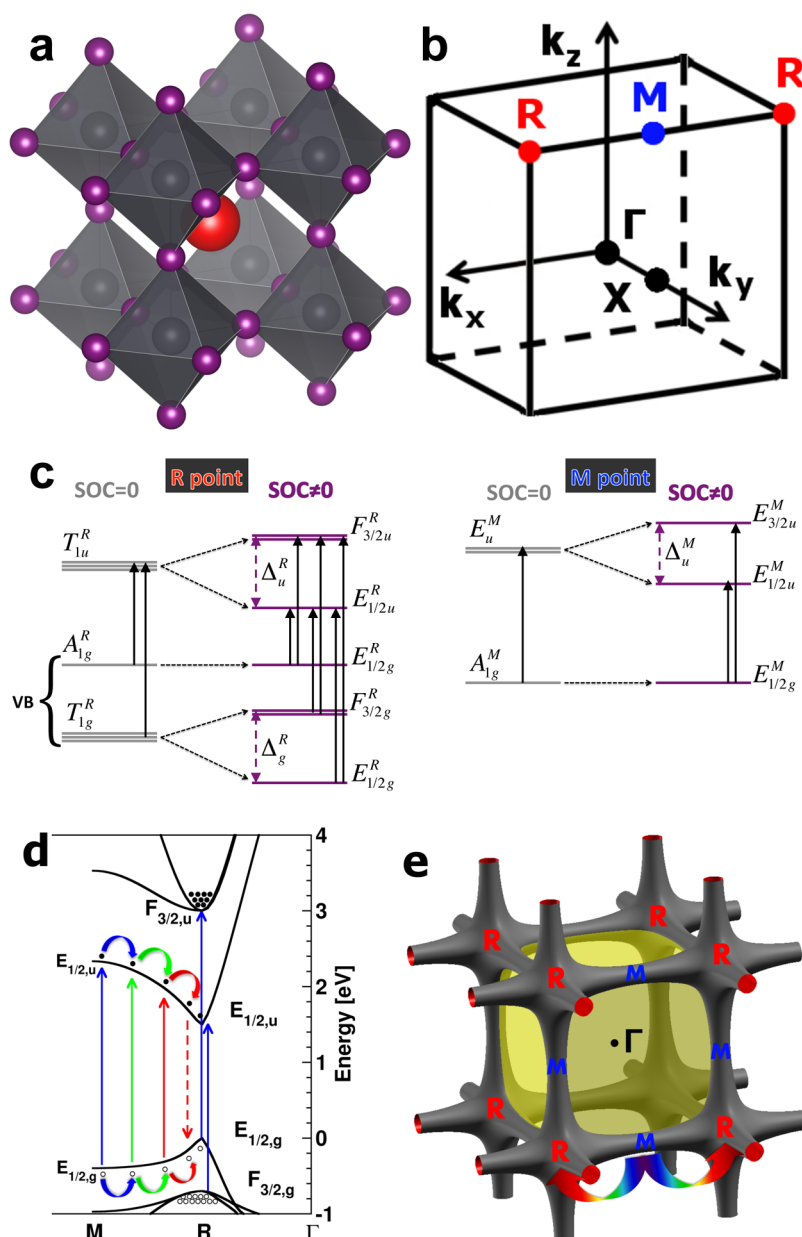


Figure 1. Analysis of optical absorption spectra of $\text{CH}_3\text{NH}_3\text{MX}_3$ based on group theory, electronic band diagram, and Fermi surface. (a) Real space 3D view of the $Pm\bar{3}m$ cubic crystal structure of metal–halide hybrid perovskites of general formulas $\text{CH}_3\text{NH}_3\text{MX}_3$. The CH_3NH_3^+ cation is located at the center of the cube with an averaged position sketched by a red ball. (b) Reciprocal space 3D view showing the first Brillouin Zone (BZ) of the $Pm\bar{3}m$ space group. Points of high symmetry in the cubic BZ are indicated by conventional letters: Γ denotes the origin of the BZ; X is the center of a square face at the BZ boundary, M is a center of a cube edge; and R are vertices of the cube. (c) Schematic energy level diagrams drawn at the high symmetry R and M points of the $Pm\bar{3}m$ BZ. Irreducible representations of the simple ($\text{SOC} = 0$, where SOC denotes spin orbit coupling) and double ($\text{SOC} \neq 0$) groups are indicated. The level splitting associated with SOC are labeled Δ_g^R , Δ_u^R , and Δ_g^M . The additional spin degeneracy is not indicated for the double group representations. The upward arrows show the symmetry allowed optical transitions. (d) Electronic band diagram of the high temperature $Pm\bar{3}m$ cubic phase of $\text{CH}_3\text{NH}_3\text{PbI}_3$ taking SOC into account; an upward energy shift of 1.4 eV has been applied to match the experimental bandgap value at R . Carrier localization and transport after optical excitation are sketched. (e) Fermi surface ($E = -0.5$ eV) in the first BZ. R and M are connected along the edges, highlighting the saddle point nature of M .

bandgap, and a 3-fold increase of the photoluminescence radiative lifetime.²⁴ Snaith and colleagues suggest localization of electrons and holes in different regions of the perovskite's unit cell but do not rule out the presence of excitons in the material following photoexcitation.²⁴ Thus, it is still unclear whether the photoexcited species are excitons or free charges. Moreover, little is known about what could make mixed halides superior to triiodide perovskites, namely, the origin of increased mobilities and decreased charge carrier recombinations that enhance PV

efficiencies. Besides, a very recent review mentions the frequency-dependence of the dielectric constant.²⁵

Here we report a theoretical investigation of a series of metal–halide perovskites: $\text{CH}_3\text{NH}_3\text{PbX}_3$, $X = \text{I}, \text{Br}, \text{Cl}$. First, we thoroughly analyze calculated absorption spectra of the reference cubic phase of lead-based compounds. Next, we discuss the nature of the photoexcited species based on extensive use and modeling of both recent and older experimental findings, namely, temperature-dependent absorp-

tion spectra,^{26,27} millimeter-wave spectroscopy,²⁸ low frequency dielectric measurements,²⁹ and NMR data related to the motion of molecular cations.³⁰ Then we discuss in sequence the impact of halogen substitution on absorption and carrier mobilities. Computational details are provided in the Supporting Information.

The ideal cubic crystal structure (*Pm3m* space group) of metal–halide perovskites is sketched in Figure 1a together with the corresponding Brillouin Zone (BZ) in reciprocal space (Figure 1b). It has been shown that symmetry analysis of this ideal cubic phase is relevant for crystal structures having a group–subgroup relationship.¹⁸ Thus, the electronic band structure of the room temperature (RT) tetragonal phase of $\text{CH}_3\text{NH}_3\text{PbI}_3$ is directly connected to that of the cubic phase.¹⁸ The latter has high symmetry points among which the R and M are of major importance to our purpose. In fact, recent calculations of the imaginary part of the dielectric function for the high temperature cubic phase of $\text{CH}_3\text{NH}_3\text{PbI}_3$, based on density functional theory (DFT) within the random-phase approximation (RPA), evidenced the onsets of primary and secondary absorptions related to R and M points, respectively.¹⁸ Similar features are obtained for $\text{CH}_3\text{NH}_3\text{PbCl}_3$ (Figure S4 in the Supporting Information). These calculations do not consider spin–orbit coupling (SOC) that induces giant splittings of the CB of lead-based hybrid perovskites.^{17,18,32} A first insight in these optical features can be gained from group theory. The symmetry analysis of the electronic states at R and M in the simple (without SOC) and double (with SOC) group allows identifying the optically allowed transitions. The simple group T_{1u} vectorial representation of the CB at R is split in a doubly degenerated $E_{1/2u}$ (spin–orbit split-off states) and a 4-fold degenerated $F_{3/2u}$ state (Figure 1c). The ground state isotropic optical transition is thus predicted at R between doubly degenerated $E_{1/2g}$ VB and $E_{1/2u}$ CB states depicted in Figure 1d for the calculated band structure. Complete diagrams with and without SOC are provided in Figures S1 and S2 (Supporting Information). At R, a series of other transitions are optically allowed, the lowest in energy corresponding to two secondary transitions $F_{3/2g} \rightarrow E_{1/2u}$ and $E_{1/2g} \rightarrow F_{3/2u}$ (Figure 1). The transition between the doubly degenerated $E_{1/2g}$ VB and $E_{1/2u}$ CB states at M is also optically allowed and transverse electric (TE). To determine which of these transitions is responsible for the peak experimentally observed at 480 nm in the absorption spectra, we evaluate the strength of the optical transitions, as defined by optical matrix elements (Tables S2 and S3 in the Supporting Information). Values are significantly larger for M, thanks to a 3-fold contribution, and the upward 1 eV energy shift is consistent with experimental findings. The 3-fold contribution can be intuited from the Fermi surface plotted in the first BZ close to the top of the VB (Figure 1e). Moreover, the different optically allowed transitions have sizable matrix elements disclosing the multibandgap nature at the origin of broad absorption of $\text{CH}_3\text{NH}_3\text{PbI}_3$, expanding from the visible to the near-IR (see also the Supporting Information).

Next, the Fermi surface (isoenergy surface below the valence band maximum at -0.5 eV, Figure 1e) reveals clear connection between R and M along the edges of the BZ. While the BZ valleys are located around R, M correspond to saddle points. This suggests that, in reciprocal space, hole carriers generated by optical absorption at M and all along the $M \rightarrow R$ paths at various wavelengths (Figure 1d) can flow easily toward R. The relaxation process may be assisted by acoustic phonons or

coupling to collective molecular rotations (*vide infra*). Contrarily, one expects that some of the carriers generated by the secondary optical transitions at R may be trapped in the $F_{3/2u}$ (CB) and $F_{3/2g}$ (VB) states (Figure 1d). Further relaxation $F_{3/2g} \rightarrow E_{1/2g}$ (holes) and $F_{3/2u} \rightarrow E_{1/2u}$ (electrons) may occur by optical phonon assisted relaxations, provided that the energy conservation rule is fulfilled. Such a “phonon bottleneck” is well-known in the case of carrier injection in semiconductor quantum dots.^{33–35} However, in quantum dots, carrier assisted (Auger relaxation) is the dominant effect in the high injection regime, yielding very fast carrier relaxation. A similar hot hole cooling (intraband process) from $F_{3/2g}$ to $E_{1/2g}$ is consistent with the relaxation after optical excitation reported for $\text{CH}_3\text{NH}_3\text{PbI}_3$.¹⁵ Similar results are obtained for the cubic *Pm3m* phase of $\text{CH}_3\text{NH}_3\text{PbCl}_3$ (Figure S3 and Tables S4 and S5 in the Supporting Information), with a larger bandgap and a larger splitting between primary (R) and secondary (M) optical transitions.

Let us now discuss the nature of the photoexcited species at room temperature. For the secondary transition at M, excitonic effects are expected to be small as a consequence of its saddle point nature (Figure 1d,e). This is consistent with the absence of excitonic features at higher energy in the spectrum recorded at 4.2 K.²⁶ If experimental studies clearly exhibit excitonic effects in the low-energy part of the absorption spectra of $\text{CH}_3\text{NH}_3\text{PbX}_3$ at low temperatures (LT),^{26,36,37} the situation is less straightforward at RT. In fact, recent experiments performed at RT have been analyzed considering free carrier transport.^{24,38,39} For instance, achievement of planar heterojunction cells has been related to low bimolecular charge recombination constants suggesting spatial separation of opposite charge carriers within the perovskite.²⁴ Next, if the exciton binding energies reported at LT (37–50 meV)^{26,36,37} remain unchanged at RT ($kT \approx 26$ meV), free charge carriers and excitons should coexist.²⁴ To gauge the importance and origin of screening we may go back to experimental data recorded two decades ago. Ishihara et al. reported absorption spectra of $\text{CH}_3\text{NH}_3\text{PbI}_3$ at different temperatures.²⁷ These data are consistent with an exciton quenching between 159 and 212 K (Figure 2), in relation with the structural transition at $T_c =$

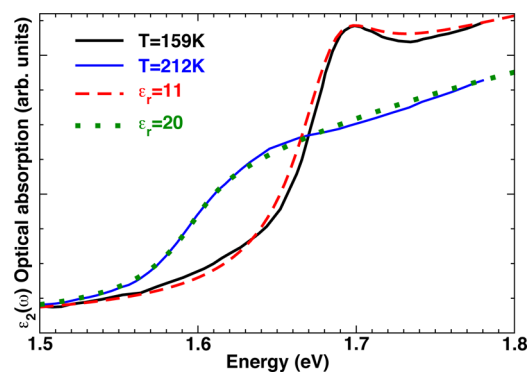


Figure 2. Optical absorption spectra of $\text{CH}_3\text{NH}_3\text{PbI}_3$ highlighting exciton screening. Experimental data taken from ref 27 recorded at 159 K (black line) and 212 K (blue line) and computed spectra for bound and continuum pair states, considering two-particle wave function and effective mass equations for electron and hole (expression 3 with $\gamma = 0.03$ eV and $\mu = 0.16m_e$). The effect of dielectric screening is shown for $\epsilon_{\text{eff}}=11$ (red dash line) and 20 (green dot line) and leads to a good fit of the experimental spectra below (159 K) and above T_c (212 K), respectively.

162 K. The exciton quenching includes both exciton screening and gap-switching^{17,18} (ill-named exciton-switching), that also appears in 2D hybrids^{27,40} (see also in the Supporting Information). This prompts the need for a better understanding of the exciton at RT.

Theoretically, excitonic effects can be accounted for using the Bethe–Salpeter equation (BSE) starting from the mono-electronic states calculated at the DFT level. When taking the high temperature cubic phases of $\text{CH}_3\text{NH}_3\text{PbCl}_3$ (Figure S4 in the Supporting Information) and $\text{CH}_3\text{NH}_3\text{PbI}_3$,¹⁸ enhancement of absorption at the bandgap is clearly evidenced. However, in the perturbative BSE approach, screening of the electron–hole interaction due to atomic motion is not taken into account. This means that experimental results cannot be fully understood from BSE calculations, if the latter effects are important. A convenient way to simulate exciton screening is to consider a two-particle wave function $\psi(r_e, r_h)$, where r_e (r_h) is the electron (hole) position.⁴¹ The effective mass approximation works well close to the bandgap in 3D hybrids both for electrons and holes,^{18,23} thanks to the giant SOC in the CB leading to a nondegenerate band instead of a triply degenerate one obtained without SOC (vide infra).¹⁷ For a Wannier exciton, the two-particle Hamiltonian including electrostatic interaction and effective mass approximation for electrons and holes reads:⁴¹

$$H = E_g - \frac{\hbar^2}{2m_e} \Delta_{r_e} - \frac{\hbar^2}{2m_h} \Delta_{r_h} - \frac{e^2}{4\pi\epsilon_{\text{eff}}|r_e - r_h|} \quad (1)$$

E_g is the bandgap energy, ϵ_{eff} the effective dielectric constant, and m_e (m_h) the electron (hole) effective mass. Introducing the center-of-mass coordinate $R = (m_e r_e + m_h r_h)/(m_e + m_h)$ and the difference coordinate $r = r_e - r_h$, the general solution becomes of separable form, $\psi(r_e, r_h) = (e^{iKR})/(\sqrt{V})\phi(r)$, where $\phi(r)$ is the wave function for the relative motion. The corresponding Hamiltonian reads:⁴¹

$$H_r = E_g - \frac{\hbar^2}{2\mu} \Delta_r - \frac{e^2}{4\pi\epsilon_{\text{eff}}r} \quad (2)$$

The reduced mass is defined by $(1/\mu) = (1/m_e) + (1/m_h)$. For the relative electron–hole motion, the Hamiltonian (eq 2) has two types of solutions. First, bound pair states of energy $E_n = E_g - (Ry)/(n^2)$ where $Ry = (\mu e^4)/(2\hbar^2(4\pi\epsilon_{\text{eff}})^2)$ is the exciton Rydberg energy, and n the quantum number ($n = 1$ for the 1S exciton ground state, $n = 2$ for the 2S exciton state, ...). The wave functions are products of spherical harmonics and Laguerre polynomials.⁴¹ The second type of solutions corresponds to a continuum of pair states having energies larger than the bandgap energy. Their wave functions are not simple planewaves but products of spherical harmonics and complex radial components related to confluent hypergeometric functions.⁴¹ Even though electron and hole states correspond to propagative states, the motions are weakly correlated. For that reason, the absorption of the continuum of pair states above the bandgap is enhanced as compared to simple band-to-band transitions when the electron–hole interaction is neglected in eq 1. This enhancement is important in the context of solar cells because carriers are generated by light over a large spectral region, especially above the bandgap. The optical absorption reads⁴¹

$$I(\tilde{E})/I_0 = 4 \sum_{n=1}^{\infty} \frac{\gamma/n^3}{(\tilde{E} + 1/n^2)^2 + \gamma^2} + \int_0^{\infty} \frac{d\tilde{E}'}{\pi} \frac{\gamma S(\tilde{E}')\sqrt{\tilde{E}'}}{(\tilde{E} - \tilde{E}')^2 + \gamma^2} \quad (3)$$

$\tilde{E} = (\hbar\omega - E_g)/(Ry)$ is a reduced energy, γ a broadening factor that depends on the temperature, and $S(\tilde{E}) = 2\pi/(\sqrt{\tilde{E}}(1 - e^{-2\pi/\sqrt{\tilde{E}}}))$ the absorption enhancement factor of the continuum of pair states. In the limit of free carriers or a totally screened interaction, the first sum (bound exciton pair states) disappears in eq 3 and $S(\tilde{E})$ reduces to 1. Simulated optical absorption spectra using eq 3 are compared to experimental data in Figure 2 (see also Figure S5 in the Supporting Information) considering different dielectric constants to highlight screening effects. Experimental absorption spectra above the critical temperature T_c are well reproduced with a larger effective dielectric constant than below T_c . It yields a reduction of the 1S exciton binding energy for all the spectra above T_c from ca. 15 to 5 meV (Figure 3). With the value of the exciton binding

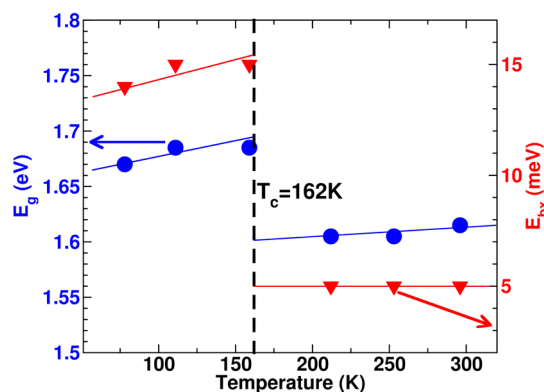


Figure 3. Electronic bandgap (left-hand axis) and exciton binding (right-hand axis) energies calculated from the experimental absorption spectra of $\text{CH}_3\text{NH}_3\text{PbI}_3$ ²⁷ using eq 3 for the computed absorption spectra (Figures 2 and S5 in the Supporting Information). Structural phase transition occurs at $T_c = 162$ K (black dashed line).

energy being smaller than kT (~ 26 meV) at room temperature, we may infer that most electron–hole pairs are ionized yielding free carriers. This also leads to ca. 80 meV shift of the electronic bandgap at T_c (Figure 3).

This prompts a comment (see also in the Supporting Information) on exciton binding energies of 37–50 meV deduced from magnetoabsorption spectroscopy measurements at liquid helium temperature.^{26,37} These values have been obtained considering the above-mentioned Wannier exciton model, with an additional contribution related to magnetic coupling. As quoted by the authors, “the only unknown parameter is the dielectric constant” ϵ_{eff} .²⁶ The choice for the high frequency dielectric constant (6.5 for $\text{CH}_3\text{NH}_3\text{PbI}_3$) was motivated by the fact that “the binding energy... is much larger than energies of optical phonon modes.”²⁶ However, from recent Raman scattering experiments, we know that this argument is not valid since optical phonons with energies as low as 8 meV (vibration of the inorganic cage) and 16 meV (libration of the organic cation) have been evidenced.⁴² This suggest that the effective dielectric constant is most probably larger due to screening induced by vibrations at low temperature. Taking $\epsilon_{\text{eff}} = 11$ as in Figure 2, the 1S exciton binding energy drops from 37–50 meV to 18–24 meV at 5 K. The latter binding energies become close to those shown Figure 3. Moreover, no 2S exciton peak was reported in the experimental spectra at liquid helium temperature.^{26,37} However, within the Wannier exciton model, eq 3, the 2S binding energy and intensity are $Ry/4$ and 8 times smaller,

respectively. Thus, the 1S–2S splitting should amount to 37 and 57 meV for $\text{CH}_3\text{NH}_3\text{PbI}_3$ and $\text{CH}_3\text{NH}_3\text{PbBr}_3$, respectively. Given the experimental resolution and spectral broadening, the 2S state should have been detected.^{26,27,37} This is also an indication that the 1S exciton binding energy was most probably overestimated.

The influence of the low temperature structural transition on the dielectric properties can be further investigated by reviewing the available data for $\text{CH}_3\text{NH}_3\text{PbI}_3$ and $\text{CH}_3\text{NH}_3\text{PbCl}_3$, summarized in Table S6 (Supporting Information, including additional discussion). These data evidence different features for the high and low frequency regimes as sketched in Figure 4. First, the high frequency

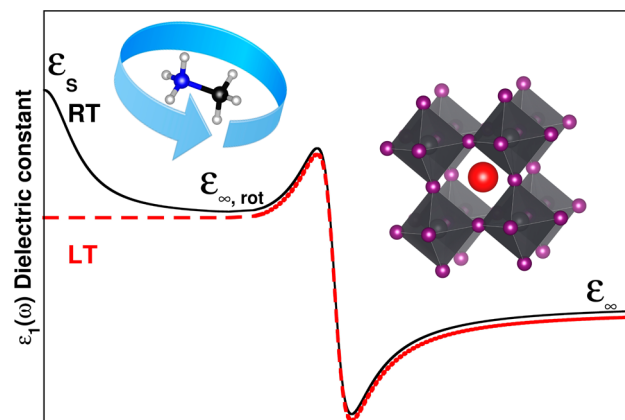


Figure 4. Schematic drawing of the dielectric constant as a function of frequency displaying respective contributions of CH_3NH_3^+ rotations and perovskite's vibrational phonons. Frequency dependence of the dielectric constant of $\text{CH}_3\text{NH}_3\text{PbX}_3$ as derived from available experimental data summarized in Table S6 (Supporting Information). The high frequency response is related to vibrational polar phonons stemming from modes of the perovskite lattice (right-hand side). The low frequency region (left-hand side) shows significant differences for the low (LT, red dash line) and room (RT, black line) temperature phases. The static dielectric constant (ϵ_s) increase at RT is primarily attributed to rotational motion of CH_3NH_3^+ cations.

behavior can be related to vibrational polar phonons of the lattice by analogy with reflectivity measurements on the all-inorganic analogue CsPbCl_3 .⁴³ From comparison of dielectric measurements at 1 kHz²⁹ and millimeter wave spectroscopy at 90 GHz,²⁸ we conclude that the high frequency vibrational contributions are little affected by the phase transition in $\text{CH}_3\text{NH}_3\text{PbX}_3$. Next, an additional contribution shows up above T_c in the low frequency range (Figure 4). We attribute this dielectric increment to the collective tumbling of cation's C–N axis at RT, evidenced by NMR,³⁰ dielectric,²⁹ and millimeter wave spectroscopies.²⁸ A similar drop in the dielectric spectra of alkali–cyanides has been reported and related to the collective tumbling of C–N– anions that get frozen in the LT phase.⁴⁴ In C_{60} fullerenes, the self-localized exciton observed at LT becomes a diffusing free exciton above a critical temperature where free rotations of C_{60} molecules are collectively activated.⁴⁵ In $\text{C}_5\text{H}_{10}\text{NH}_2\text{PbI}_3$, a 1D hybrid perovskite, strongly bound excitons are formed, self-trapped by deforming the lattice in their neighborhood,⁴⁶ but with a clear Stokes shift (1.2 eV), which is not observed in 3D compounds like $\text{CH}_3\text{NH}_3\text{PbI}_3$. It is worth mentioning that among the all-inorganic perovskites CsPbX_3 , CsPbI_3 is the only one exhibiting a self-trapped exciton at LT with a sizable Stokes

shift (0.74 eV).⁴⁷ In addition, our simulated absorption spectra around T_c (Figure 2) and our analysis of liquid helium experimental results indicate that the effective dielectric constant is somewhat larger than its high frequency limit ($\epsilon_\infty \approx 6.5$) below T_c , suggesting possible exciton screening by polar modes. For $\text{CH}_3\text{NH}_3\text{PbX}_3$, we can thus conclude that the LT exciton resonance is related to a Wannier like exciton already partially screened by polar modes, which becomes completely screened above T_c , yielding almost free carriers when the orientational motions of the cations are collectively activated by a structural phase transition.

In the cubic $\text{CH}_3\text{NH}_3\text{PbX}_3$ hybrid perovskites, each CH_3NH_3^+ cation is located in a cuboctahedral cage formed by the 12 nearest halogen atoms. The size of this cage reduces when iodine is substituted by chlorine (–25%), leading to restricted molecular motion.²⁸ Thus, the drop in dielectric constant is larger for iodine-based compounds. It shows up in different Lorentz local field factors evidencing the different dielectric environments in both compounds.²⁸ A similar variation of cell volume is observed between KCN and NaCN crystals, with a smaller cell for the latter,⁴⁸ leading to a glassy disorder for CN^- ions and local strain in mixed crystals. The different behavior of the reorientation dynamics of CN^- between these two alkali–cyanides has been attributed to both the smaller size of the NaCN lattice and to reduced polarizability for Na^+ as compared to K^+ . Moreover, it has been shown that the CN^- collective ordering is severely affected by insertion of alkali metals of another size. The cationic impurities strongly hinder rotation of CN^- ions that are prevented to take part in the collective process. We propose in this work that a comparable effect appears upon halogen doping in 3D hybrid perovskites. If collective tumbling of CH_3NH_3^+ is hampered, exciton screening will be reduced leading to a sizable increase in absorption. Such enhancement of absorption upon Cl doping has been evidenced in $\text{CH}_3\text{NH}_3\text{PbI}_3$ ^{21,24} and $\text{CH}_3\text{NH}_3\text{PbBr}_3$.⁴⁹ Further studies at low temperature by time-resolved photoluminescence, pump–probe experiments, or dielectric measurements should allow to confirm this point.

Molecular motions that affect electron–hole interactions is also expected to change the drift–diffusion current for electrons and holes. At high temperature ($T > T_c$), tumbling of CH_3NH_3^+ cations may couple to carrier mobility in the perovskite crystal. Indeed, at RT, current–voltage characteristics of $\text{CH}_3\text{NH}_3\text{PbI}_3$ exhibit a ferroelectric hysteresis attributed to the reorientation of the permanent dipoles of CH_3NH_3^+ on application of an external electric field in addition to the resistance of the inorganic lattice.³¹ Polarization measurements and analysis of the coercive field in the current–voltage hysteresis loops are also in favor of charge motion within the material.³¹ Chlorine doping might restrict collective rotations of the CH_3NH_3^+ and consequently increase electron–hole diffusion lengths for $\text{CH}_3\text{NH}_3\text{PbI}_{3-x}\text{Cl}_x$ as compared to $\text{CH}_3\text{NH}_3\text{PbI}_3$. Such interpretation is consistent with experimental findings.^{14,24} The morphology of hybrid perovskite grains is also important for transport properties. Intergranular barriers, rather than intrinsic mechanisms, probably dominate carrier transport in highly disordered samples, and different grain sizes may result from alloys in such compounds. However, in high quality samples substantial charge carrier mobility losses at grain boundaries do not prevail.²⁴

In summary, this work indicates that the broad light-harvesting abilities of the inorganic–organic family of perovskites $\text{CH}_3\text{NH}_3\text{MX}_3$, recently used for high-performance solar cells, is a direct consequence of their multibandgap and multivalley nature. In some sense, they can be thought as natural multijunction. The low energy absorption peak at 760 nm in $\text{CH}_3\text{NH}_3\text{PbI}_3$ is attributed to the direct bandgap transition at the high-symmetry point R from the VB maximum to CB minimum. The peak located at 480 nm corresponds mainly to a direct transition at M, with additional contributions from secondary direct transitions at R. Moreover, the carriers redistribution after optical excitation is facilitated by a channel from R to M. Inspection of the dielectric responses over a wide frequency range allows clarifying the nature of the photoexcited species created in these materials. In particular, as shown in this work, the Wannier-like exciton evidenced at low temperature becomes almost entirely screened at room temperature, yielding free carriers, due to optical phonons and collective rotational motion of the organic cations. In mixed halide perovskites, the insertion of a halide of another size is suggested to prevent such collective reorientations, thus reducing exciton screening and enhancing optical absorption. This picture is also consistent with the counterintuitive increase of carrier mobility experimentally evidenced upon doping.^{14,24} In fact, the local lattice disorder brought by alloying should reduce electron–hole diffusion lengths. However, doping might restrict molecular motion and enhance transport properties. Low temperature time-resolved photoluminescence, pump–probe experiments should be able to confirm the impact of the phase transition on the exciton screening. Dielectric measurements on mixed lead–halide perovskites may also help to clarify the role of halide doping on the collective rotational motion.

■ ASSOCIATED CONTENT

■ Supporting Information

Computational details, additional details, and discussions for theoretical models, electronic band structures, absorption spectra, gap (exciton) switching, and dielectric properties. This material is available free of charge via the Internet at <http://pubs.acs.org>.

■ AUTHOR INFORMATION

Corresponding Authors

*(J.E.) E-mail: jacky.even@insa-rennes.fr. Tel: +33 (0)2 23 23 82 95.

*(C.K.) E-mail: claudine.katan@univ-rennes1.fr. Tel: +33 (0)2 23 23 56 82.

Notes

The authors declare no competing financial interest.

■ ACKNOWLEDGMENTS

This work was performed using HPC resources from GENCI-CINES/IDRIS grant 2013-c2012096724. The work is supported by Agence Nationale pour la Recherche (PEROCAI project ANR-10-04).

■ REFERENCES

- (1) Shockley, W.; Queisser, H. J. Detailed balance limit of efficiency of p–n junction solar cells. *J. Appl. Phys.* **1961**, *32*, 510–519.
- (2) Green, M. A.; Emery, K.; Hishikawa, Y.; Warta, W.; Dunlop, E. D. Solar cell efficiency tables (version 42). *Prog. Photovolt. Res. Appl.* **2013**, *21*, 827–837.

- (3) Friedman, D. J. Progress and challenges for next-generation high-efficiency multijunction solar cells. *Curr. Opin. Solid State Mater. Sci.* **2010**, *14*, 131–138.

- (4) Kojima, A.; Teshima, K.; Shirai, Y.; Miyasaka, T. Organometal halide perovskites as visible-light sensitizers for photovoltaic cells. *J. Am. Chem. Soc.* **2009**, *131*, 6050–6051.

- (5) Lee, M. M.; Teuscher, J.; Miyasaka, T.; Murakami, T. N.; Snaith, H. J. Efficient hybrid solar cells based on meso-superstructured organometal halide perovskites. *Science* **2012**, *338*, 643–647.

- (6) Kim, H.-S.; Lee, C. R.; Im, J. H.; Lee, K. B.; Moehl, T.; Marchioro, A.; Moon, S. J.; Humphry-Baker, R.; Yum, J. H.; Moser, J. E.; Grätzel, M.; Park, N. G. Lead iodide perovskite sensitized all-solid-state submicron thin film mesoscopic solar cell with efficiency exceeding 9%. *Sci. Rep.* **2012**, *2*, 591.

- (7) Heo, J. H.; Im, S. H.; Noh, J. H.; Mandal, T. N.; Lim, C. S.; Chang, J. A.; Lee, Y. H.; Kim, H. J.; Sarkar, A.; Nazeeruddin, M. K.; Grätzel, M.; Seok, S., II. Efficient inorganic–organic hybrid heterojunction solar cells containing perovskite compound and polymeric hole conductors. *Nat. Photonics* **2013**, *7*, 486–491.

- (8) Burschka, J.; Pellet, N.; Moon, S. J.; Humphry-Baker, R.; Gao, P.; Nazeeruddin, M. K.; Grätzel, M. Sequential deposition as a route to high-performance perovskite-sensitized solar cells. *Nature* **2013**, *499*, 316–319.

- (9) Kim, H.-S.; Mora-Sero, I.; Gonzalez-Pedro, V.; Fabregat-Santiago, F.; Juarez-Perez, E. J.; Park, N. G.; Bisquert, J. Mechanism of carrier accumulation in perovskite thin-absorber solar cells. *Nat. Commun.* **2013**, *4*, 2242.

- (10) Park, N. G. Organometal perovskite light absorbers toward a 20% efficiency low-cost solid-state mesoscopic solar cell. *J. Phys. Chem. Lett.* **2013**, *4*, 2423–2429.

- (11) Noh, J. H.; Im, S. H.; Heo, J. H.; Mandal, T. N.; Seok, S. I. Chemical management for colorful, efficient, and stable inorganic–organic hybrid nanostructured solar cells. *Nano Lett.* **2013**, *13*, 1764–1769.

- (12) Liu, M.; Johnston, M. B.; Snaith, H. J. Efficient planar heterojunction perovskite solar cells by vapour deposition. *Nature* **2013**, *501*, 395–398.

- (13) Snaith, H. J. Perovskites: The emergence of a new era for low-cost, high-efficiency solar cells. *J. Phys. Chem. Lett.* **2013**, *4*, 3623–3630.

- (14) Stranks, S. D.; Eperon, G. E.; Grancini, G.; Menelaou, C.; Alcocer, M. J. P.; Leijtens, T.; Herz, L. M.; Petrozza, A.; Snaith, H. J. Electron-hole diffusion lengths exceeding 1 micrometer in an organometal trihalide perovskite absorber. *Science* **2013**, *342*, 341–344.

- (15) Xing, G.; Mathews, N.; Sun, S.; Lim, S. S.; Lam, Y. M.; Grätzel, M.; Mhaisalkar, S.; Sum, T. C. Long-range balanced electron- and hole-transport lengths in organic–inorganic $\text{CH}_3\text{NH}_3\text{PbI}_3$. *Science* **2013**, *342*, 344–347.

- (16) Loi, M. A.; Hummelen, J. C. Hybrid solar cells: Perovskites under the sun. *Nat. Mater.* **2013**, *12*, 1087–1089.

- (17) Even, J.; Pedesseau, L.; Jancu, J.-M.; Katan, C. Importance of spin–orbit coupling in hybrid organic/inorganic perovskites for photovoltaic applications. *J. Phys. Chem. Lett.* **2013**, *4*, 2999–3005.

- (18) Even, J.; Pedesseau, L.; Jancu, J.-M.; Katan, C. DFT and $k \cdot p$ modelling of the phase transitions of lead and tin halide perovskites for photovoltaic cells. *Phys. Status Solidi RRL* **2014**, *8*, 31–35.

- (19) Brivio, F.; Walker, A. B.; Walsh, A. Structural and electronic properties of hybrid perovskites for high-efficiency thin-film photovoltaics from first-principles. *Appl. Phys. Lett. Mater.* **2013**, *1*, 042111.

- (20) Baikie, T.; Fang, Y.; Kadro, J. M.; Schreyer, M.; Wei, F.; Mhaisalkar, S. G.; Grätzel, M.; White, T. J. Synthesis and crystal chemistry of the hybrid perovskite $(\text{CH}_3\text{NH}_3)\text{PbI}_3$ for solid-state sensitised solar cell applications. *J. Mater. Chem. A* **2013**, *1*, 5628–5641.

- (21) Colella, S.; Mosconi, E.; Fedeli, P.; Listorti, A.; Gazza, F.; Orlandi, F.; Ferro, P.; Besagni, T.; Rizzo, A.; Calestani, G.; Gigli, G.; De Angelis, F.; Mosca, R. $\text{MAPbI}_{3-x}\text{Cl}_x$ mixed halide perovskite for

hybrid solar cells: The role of chloride as dopant on the transport and structural properties. *Chem. Mater.* **2013**, *25*, 4613–4618.

(22) Mosconi, E.; Amat, A.; Nazeeruddin, M. K.; Grätzel, M.; De Angelis, F. First-principles modeling of mixed halide organometal perovskites for photovoltaic applications. *J. Phys. Chem. C* **2013**, *117*, 13902–13913.

(23) Giorgi, V.; Fujisawa, J.-I.; Segawa, H.; Yamashita, K. Small photocarrier effective masses featuring ambipolar transport in methylammonium lead iodide perovskite: A density functional analysis. *J. Phys. Chem. Lett.* **2013**, *4*, 4213–4216.

(24) Wehrenfennig, C.; Eperon, G. E.; Johnston, M. B.; Snaith, H. J.; Herz, L. M. High charge carrier mobilities and lifetimes in organolead trihalide perovskites. *Adv. Mater.* **2014**, *26*, 1584–1589.

(25) Kim, H. S.; Im, S. H.; Park, N.-G. Organolead Halide Perovskite: New Horizons in Solar Cell Research. *J. Phys. Chem. C* **2014**, *118*, 5615–5625.

(26) Hirasawa, M.; Ishihara, T.; Goto, T.; Uchida, K.; Miura, N. Magnetoabsorption of the lowest exciton in perovskite-type compound (CH₃NH₃)PbI₃. *Phys. B* **1994**, *201*, 427–430.

(27) Ishihara, T. Optical properties of PbI-based perovskite structures. *J. Lumin.* **1994**, *60&61*, 269–274.

(28) Poglitsch, A.; Weber, D. Dynamic disorder in methylammoniumtrihalogenoplumbates (II) observed by millimeter-wave spectroscopy. *J. Chem. Phys.* **1987**, *87*, 6373–6378.

(29) Onoda-Yamamuro, N.; Matsuo, T.; Suga, H. Dielectric study of CH₃NH₃PbX₃ (X = Cl, Br, I). *J. Phys. Chem. Solids* **1992**, *53*, 935–939.

(30) Wasylishen, R. E.; Knop, O.; Macdonald, J. B. Cation rotation in methylammoniumlead halides. *Solid State Commun.* **1985**, *56*, 581–582.

(31) Stoumpos, C. C.; Malliakas, C. D.; Kanatzidis, M. G. Semiconducting tin and lead iodide perovskites with organic cations: Phase transitions, high mobilities, and near-infrared photoluminescent properties. *Inorg. Chem.* **2013**, *52*, 9019–9038.

(32) Even, J.; Pedesseau, L.; Dupertuis, M.-A.; Jancu, J.-M.; Katan, C. Electronic model for self-assembled hybrid organic/perovskite semiconductors: Reverse band edge electronic states ordering and spin-orbit coupling. *Phys. Rev. B* **2012**, *86*, 205301.

(33) Ferreira, R.; Bastard, G. Phonon-assisted capture and intradot Auger relaxation in quantum dots. *Appl. Phys. Lett.* **1999**, *74*, 2818–2820.

(34) Ohnesorge, B.; Albrecht, M.; Oshinowo, J.; Forchel, A.; Arakawa, Y. Rapid carrier relaxation in self-assembled In_xGa_{1-x}As/GaAs quantum dots. *Phys. Rev. B* **1996**, *54*, 11532–11538.

(35) Miska, P.; Even, J.; Marie, X.; Dehaese, O. Electronic structure and carrier dynamics in InAs/InP double-cap quantum dots. *Appl. Phys. Lett.* **2009**, *94*, 061916.

(36) Kitazawa, N.; Watanabe, Y.; Nakamura, Y. Optical properties of CH₃NH₃PbX₃ (X = halogen) and their mixed-halide crystals. *J. Mater. Sci.* **2002**, *37*, 3585–3587.

(37) Tanaka, K.; Takahashi, T.; Ban, T.; Kondo, T.; Uchida, K.; Miura, N. Comparative study on the excitons in lead-halide-based perovskite-type crystals CH₃NH₃PbBr₃ CH₃NH₃PbI₃. *Solid State Commun.* **2003**, *127* (9–10), 619–623.

(38) Edri, E.; Kirmayer, S.; Mukhopadhyay, S.; Gartsman, K.; Hodes, G.; Cahen, D. Elucidating the charge carrier separation and working mechanism of CH₃NH₃PbI_{3-x}Cl_x perovskite solar cells. *Nat. Commun.* **2014**, *5*, 3461.

(39) Xing, G.; Mathews, S.; Lim, S. S.; Yantara, N.; Liu, X.; Sabba, D.; Grätzel, M.; Mhaisalkar, S.; Sum, T. C. Low-temperature solution-processed wavelength-tunable perovskites for lasing. *Nat. Mater.* **2014**, *13*, 476–480.

(40) Pedesseau, L.; Jancu, J.-M.; Rolland, A.; Deleporte, E.; Katan, C.; Even, J. Electronic properties of 2D and 3D hybrid organic/inorganic perovskites for optoelectronic and photovoltaic applications. *Opt. Quant. Electron.* **2013**, DOI: 10.1007/s11082-013-9823-9.

(41) Chuang, S. *Physics of Optoelectronic Devices*; Goodman, J. W., Ed.; Wiley: New York, 1995.

(42) Quarti, C.; Grancini, G.; Mosconi, E.; Bruno, P.; Ball, J. M.; Lee, M. M.; Snaith, H. J.; Petrozza, A.; De Angelis, F. The Raman spectrum

of the CH₃NH₃PbI₃ hybrid perovskite: interplay of theory and experiment. *J. Phys. Chem. Lett.* **2014**, *5*, 279–284.

(43) Hirotsu, S. Far-infrared reflectivity spectra of CsPbCl₃. *Phys. Lett. A* **1972**, *41*, 55–56.

(44) Ortiz-Lopez, J. Dipolar reorientation and order-disorder behavior of pure and mixed alkali cyanides. *Phys. Rev. Lett.* **1983**, *50*, 1289–1292.

(45) Matus, M.; Kuzmany, H.; Sohmen, E. Self-trapped polaron exciton in neutral fullerene C₆₀. *Phys. Rev. Lett.* **1992**, *68*, 2822–2825.

(46) Nagami, A.; Okamura, K.; Ishihara, T. Optical properties of a quantum wire crystal, C₅H₁₀NH₂PbI₃. *Phys. B* **1996**, *227*, 346–348.

(47) Nikl, M.; Nitsch, K.; Chval, J.; Somma, F.; Phani, A. R.; Santucci, S.; Giampaolo, C.; Fabeni, P.; Pazzi, G. P.; Feng, X. Q. Optical and structural properties of ternary nanoaggregates in CsI–PbI₂ co-evaporated thin films. *J. Phys.: Condens. Matter.* **2000**, *12*, 1939–1946.

(48) Ortiz-Lopez, J.; Lüty, F. Dielectric studies of CN[−] dipolar reorientation and order–disorder behavior in RbCN_{1-x}:KCN_x and KCN_{1-x}:NaCN_x. *Phys. Status Solidi B* **2001**, *228*, 893–917.

(49) Edri, E.; Kirmayer, S.; Kulbak, M.; Hodes, G.; Cahen, D. Chloride inclusion and hole transport material doping to improve methyl ammonium lead bromide perovskite-based high open-circuit voltage solar cells. *J. Phys. Chem. Lett.* **2014**, *5*, 429–433.